PHOTO REPAIR AND 3D STRUCTURE
FROM FLATBED SCANNERS

Ruggero Pintus

CRS4 (Center for Advanced Studies, Research and Development in Sardinia), Parco Scientifico e Tecnologico, POLARIS Edificio 1, 09010 Pula (CA), Italy

Thomas Malzbender

Hewlett-Packard Laboratories, 1501 Page Mill Road, Palo Alto, CA 94304, U.S.A.

Oliver Wang

University of California, Santa Cruz, 1156 High Street, Santa Cruz, CA 95064, U.S.A.

Ruth Bergman, Hila Nachlieli, Gitit Ruckenstein

Hewlett-Packard Laboratories, Technion City, Haifa 32000, Israel

Keywords: Scanners, 3D reconstruction, Photo repair, Photometric stereo.

Abstract: We introduce a technique that allows 3D information to be captured from a conventional flatbed scanner. The technique requires no hardware modification and allows untrained users to easily capture 3D datasets. Once captured, these datasets can be used for interactive relighting and enhancement of surface detail on physical objects. We have also found that the method can be used to scan and repair damaged photographs. Since the only 3D structure on these photographs will typically be surface tears and creases, our method provides an accurate procedure for automatically detecting these flaws without any user intervention. Once detected, automatic techniques, such as infilling and texture synthesis, can be leveraged to seamlessly repair such damaged areas. We first present a method that is able to repair damaged photographs with minimal user interaction and then show how we can achieve similar results using a fully automatic process.

1 INTRODUCTION

Flatbed scanners are commonly available, low cost, and commercially mature products that allow users to digitize documents and photographs efficiently. Recently, flatbed scanner products that incorporate two separate and independently controlled illumination bulbs have become available (HP, 2007). The original intent of such a two bulb design is to improve color fidelity by illuminating the document or photograph with separate chromatic spectra, effectively making a 6 channel measurement of color instead of the conventional 3 channel measurement, improving color fidelity. We demonstrate that such hardware can also be used to estimate geometric information, namely surface

normals, by a novel approach to photometric stereo.

These extracted surface normals can be used in several ways. Scanned objects can be relit interactively, effectively conveying a sense of 3D shape. Normal information can also be used to automatically repair damaged surfaces of old photographs. We have found that tears and creases in old photographs can be reliably detected since they are associated with surface normals that are not strictly perpendicular to the surface of the scanner plate. Once detected, these imperfect pixels can be replaced by leveraging infilling and texture synthesis methods, effectively repairing the print in an automatic manner. Although products do exist on the market that specialize in recovery of 3D information from physical objects, these are 2-4

Figure 1: Left: Original scan of a damaged photograph. Middle: 3D structure present on the surface of the print extracted by our method. Right: Automatically repaired photograph using 3D structure information and infilling methods.

orders of magnitude more expensive than commercial flatbed scanners and involve significant mechanical complexity. Our method requires no hardware modification to current products, no additional user interaction, and can scan objects in a very short amount of time.

Section 2 provides an overview of related work. Section 3 presents the entire procedure used to estimate the surface gradient from a flatbed scanner with two bulbs. Sections 4 and 5 describe the photograph repair application and the automatic process to remove tears and creases. Two methods are presented, one that works on two pairs of images with an intermediate manual rotation, and another method that achieves fully automatic repair from a single pair of images. Section 6 summarizes other applications and Section 7 provides paper summary and conclusions.

2 RELATED WORK

In this paper, we use principles from photometric stereo to recover per-pixel surface normals of a 3D object or photograph. The recent introduction of flatbed scanners that employ 2 separately controlled light sources greatly facilitates this approach (fig.2). As an alternative approach to gathering 3D structure from flatbed scanners, (Schubert, 2000) demonstrates how they can be used to collect stereoscopic images. Although no explicit extraction of depth or 3D information is performed, a good percept of 3D shape can be achieved with this approach. Schubert leverages the fact that in such CCD-based scanners, the resulting scanned images perform a orthographic projection in the direction of the carriage movement, y, but a perspective projection in the orthogonal direction, x. By repositioning the object with variation in the x placement, views of the object from multiple perspectives are achieved. Stereograms can be produced to good effect by arranging and viewing these images appropriately.

Although the hardware prototype has significantly more complexity than a flatbed scanner, (Gardner et al., 2003) shows an elegant approach using Lego Mindstorm and linear light sources to collect normal and albedo information, along with higher-order reflectance properties. This approach can not be leveraged on today's flatbed scanners due to the fixed geometric relationship between the light sources and imagers in conventional scanners. A related, unpublished approach was independently developed by (Chantler and Spence, 2004). Their acquisition methodology is similar, and also discusses the approach of simultaneously performing registration and photometric stereo. However, applications such as photo repair and reflectance transformation are not pursued. (Brown et. al, 2008) describe an approach for digitizing geometry, normals and albedo of wall painting fragments using the combination of a 3D scanner and a conventional flatbed scanner. Surface normals are acquired with a flatbed scanner by combining 2D scans. They demonstrate the improved normal fidelity that can be achieved by photometric stereo as opposed to 3D scanning.

Our image repair application is motivated by earlier work on removing dust and scratch from scanned images. (Bergman et al., 2007) describe a range of solutions for dust and scratch removal. For scans of transparent media, i.e. negative or slides, (DIGITAL ICE, 2001) introduced the use of Infra-red (IR) hardware. The IR light is blocked by dust and scattered by scratches, thereby enabling very accurate defect detection. For prints, detection is based upon characteristics of the defects in the digital image, e.g., defects that are light and narrow.

While this approach correctly identifies defects, it is prone to false detection of image features with

similar characteristics. We propose a detection method for scanned prints based on 3D surface normals.
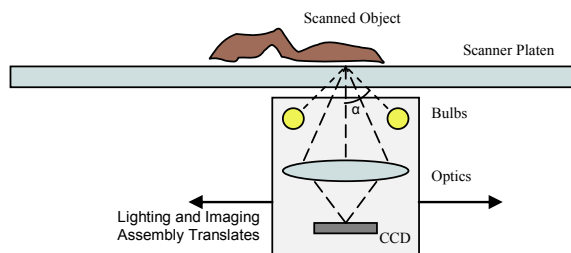

Figure 2: Typical flatbed scanner – side view. Note the lighting assembly moves with the imager, effectively providing two lighting directions across the entire scan.

Figure 3: Images captured by our modified HP Scanjet 4890. Pairs of scans are captured with only one of two bulbs actuated independently. For the second pair, the user has manually rotated the fossil by roughly 90 degrees. This effectively yields 4 lighting directions.
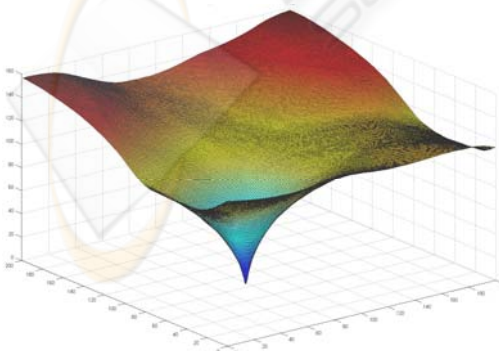

Figure 4: Prediction error for the fossil shown in Fig. 2 using the SIRPH algorithm. X: rotation, Y: translation in y, Z: error.

3 NORMAL CAPTURE FROM FOUR IMAGES

Given at least 3 images of a surface taken with different lighting directions, it is possible to recover per-pixel estimates of surface normals and albedo using photometric stereo. Flatbed scanners currently capture a single image under static lighting conditions, but they often employ 2 bulbs to illuminate the subject. These two bulbs provide illumination from either side of the scan line being imaged. If we independently control these 2 bulbs, the scanner is capable of taking 2 scans, effectively one with lighting from above, and another with lighting from below. We have experimented with two hardware platforms that allow such scans to be acquired. First, we modified an HP Scanjet 4890 to allow us to manually activate each of the two bulbs separately. Later, when the HP ScanJet G4050 became available with separate control of each bulb supported in software, we switched to this platform.

Both platforms provide 2 images with different lighting. For the first approach we describe, we retrieve another pair of images under new lighting directions by prompting the user to manually rotate the object they are scanning by roughly 90 degrees. At this point, two new scans are taken, again with each bulb activated independently yielding 4 images of the object with 4 different light source direction (fig.3). However, the two sets of images are not registered relative to each other, so we have introduced a difficult registration problem since the images are all taken under varying lighting directions. We have developed a method to robustly solve this registration problem called SIRPH, which stands for SImultaneous Registration and PHotometric stereo.

In section 4.2 we present a method that avoids any approximate manual rotation and works directly with just 2 images.

SIRPH exactly solves for the two translation and one rotation parameters, (x,y,θ), that are introduced by the user rotating the object by roughly 90 degrees. At the same time, it solves for the surface orientation (normals) at each pixel. The SIRPH method initializes the rotation and translation parameters, then uses photometric stereo (Barsky et al., 2003) on three of the images to compute surface albedo and normals per pixels. Two of the images used are from one set of scans and a third is taken from the other set which is rotated and translated according to the current best guess of the rotation and translation parameters. Photometric stereo gives us an estimation of normals and albedo of the

scanned object, which can be used to estimate the 4th image by the Lambertian reflectance model:

$$I' = \rho(N \bullet L) \tag{1}$$

where ρ is surface albedo, N is normal vector and L is the vector pointing to the light source. The estimated image, I', is then compared to the actual 4th image, I^{4}, giving us a prediction error (fig.4) for parameters (x, y, θ) as follows:

$$E_{prediciton} = \sum_{p \subset P}(I'_p - I^4_p)^2 \tag{2}$$

where P is the set of all pixels in an image, and I_p corresponds to the pth pixel in image I.

Fortunately, this prediction error is typically well behaved, and iterative nonlinear optimization techniques can be employed to find the well defined minimum. After experimenting with several nonlinear optimization methods, namely Levenberg-Marquart, Gauss-Newton and Simplex, we finally settled on a simple hierarchical approach that was both robust and fast. In our technique, we perform an iterative search starting at a low resolution working up to the original size image. At each resolution level, samples are taken at the current position and at a +/- step size increment in each of the 3 dimensions of our search space. The lowest error of these 8 + 1 sample points is chosen as the base for the next iteration. If the same base point is chosen, the step size is halved and further iterations are taken. Once the step size is below a threshold, convergence is achieved and we start the search at the next resolution level with the current convergence state. At each level, this technique is commonly known as compass-search.

Because compass-search can get stuck in local minima, a good starting point is key to convergence. We therefore perform the entire search multiple times at the lowest resolution, each "seeded" with a different starting point. Because the optimization occurs very quickly at low resolution, we are able to use many different starting points that cover a large area of the sample space. We then take the best match from all these to start the search at the next level. After we converge on the original resolution image, we will have robustly recovered the required translation and rotation parameters to register the 2 pairs of images, as well as a surface normal per pixel. We tested this method on a variety of objects and notice that it is capable of achieving correct convergence in almost all cases, including very difficult ones such as circular objects with low amounts of texture.

4 PHOTOGRAPH REPAIR APPLICATION

We have outlined our procedure for extracting 3D normals and albedo from objects using a flatbed scanner. We now present several applications of this method, the most significant being the automatic detection and repair of creases and tears in scanned photographs. Almost everyone has a one of a kind photo of their child, parent or grandparent that has been battered over the years. Old photographs often have tears, creases, stains, scratches and dust. Fortunately, the technology to restore such images exists today through a variety of digital imaging tools. Your local photo-finishing lab can do it for a fee. It can also be done in the home using a scanner, printer and photo editor such as Adobe Photoshop. This path to photo restoration is fairly tedious and requires some expertise in the use of the photo editor.

Although a reliable capability exists already to detect and repair defects in transparencies such as dust and scratches (using IR illumination), no such robust counterpart exists for the detection and repair of damaged prints. Infilling techniques from the transparency domain can be leveraged for the repair process, but the robust detection of damaged regions of a print is lacking. Our method provides such a capability, since the damage one that is looking for is associated with 3D perturbations. Figure 1 shows one example of this capability that we have prototyped with a HP 4890 scanner. The next two sections describe the procedures used for this application. We first present the 4 image procedure, which has the drawback that it requires the user to rotate the photograph. In section 4.2 we introduce a 2 image process that performs the same task, but without any user intervention.

4.1 Defect Maps from Normals

The 3D normals give a general indication of the location of the defects in the scans. In principle, high normal perturbations from the z axis (defined to be pointing up from the photograph) indicate a defect, and low normal perturbations indicate undamaged portions of the print. However, simply taking a threshold of such perturbations produces a defect map with insufficient accuracy.

This map may miss portions of the defect, e.g., very fine portions of a crease, and it is likely to have some false detections, e.g., the red pixels near the boy's left sleeve in Figure 5 (left). To overcome these issues, we use a two step approach. We first

Figure 5: Constructing defect maps using the 4-image procedure. Left: Expansion labeling computed from the normals. Right: Refinement detection map for light defects.

expand the set of candidate pixels, along features such as creases, then apply a refinement stage on the expanded mask to select a subset of these pixels that will need repair. The expansion phase thresholds the 3D normal information at two levels. Pixels with very high normal perturbations are marked as defective. Pixels with less high normal perturbations are marked as candidates. A voting algorithm, closely related to (Medioni, 2000), extends the defects. Connected components of the marked pixels are computed. Each component exerts a field of influence based on its shape and size. For example, a crease extends a field in the direction of the crease. The fields of influence from all the components are added for an overall vote at each pixel. Defective pixels are marked pixels with high votes and unmarked, connected pixels with very high votes.

The purpose of the refinement step is to select a subset of pixels identified in the expansion phase as the final selection that will require repair. The refinement step uses a grayscale representation of the image and creates a smoothed reference image that does not contain the defects by applying a median filter. Defective pixels can either be too light or too dark. In both cases the difference between the grayscale representation and the reference image is significant for defective pixels. Thresholding the difference image is prone to detection of some small, bright image features, hence we label pixels as defective only if they are both in the expanded set of candidate pixels and yield a big difference between the grayscale and reference images. We further refine the defect map by detecting the contour of the defect using classification. Looking at a neighborhood near a defect we have gray-level data and a label for each pixel of clean, defect-light or defect-dark. We label several pixels around the contour of the defect as unknown and classify them using Quadratic Discriminant Analysis (Hastie et al.,

2001). Without contour classification, a trace of the tear would remain after repair.

This refinement step is repeated once for light defects and again for dark defects. From a normal viewing distance the white areas are the most striking defect. A closer look usually reveals dark shadows adjacent to the white tear. Indeed, if we only repair the white defects, we are left with an apparent crease in the image due to the shadowed pixels. We obtained the best results by detecting and repairing (infilling) light defects and then detecting and repairing dark defects.

4.2 Normal Components from Two Images

The 4-image procedure has the drawback that the user must rotate the photograph to compute normals (or both surface derivatives along x and y). It is well known that photometric stereo requires at least three images for a complete gradient computation (Barsky et al., 2003). We have developed a method to use two images to estimate one component of the derivative (in our case the derivative along y, i.e. along image columns). In this way, we avoid needing the user to rotate the sample manually. However, we encounter two limitations. First, we have less information to detect defects, and second, the algorithm can't recover tears and creases that are precisely aligned with the image columns. We can address the first issue with a more complex procedure. To avoid perfectly vertical defects, we recommend that the user reorient the photo in the scanner.

An unmodified, commercial HP ScanJet G4050 scanner, which we used for these experiments, introduces the further complication that the chromatic spectra of each bulb is intentionally designed to be different. As mentioned, this was done to improve color fidelity effectively making a 6 channel measurement of color. This chromatic difference is problematic for photometric stereo. We overcome this issue by recovering 2 separate 3x1 color transform matrices that map each image into a similar one dimensional 'intensity' space, in which we perform photometric stereo computations. These color transform matrices have been derived by scanning a Macbeth color chart exposed with each bulb independently, and then minimizing the difference in transformed response.

A second problem with flatbed scanners is that the mechanical repeatability of the scan mechanism is not perfect, causing slight vertical misalignment between the pair of scans. To correct this we

upsample each scanned image in the vertical direction, and then we find the misalignment by minimizing the integral of the surface gradient in y direction.

We approximate the lighting geometry with lighting direction vectors

$$\begin{cases} l_1 = \begin{bmatrix} \sin\alpha_1\cos\beta_1 & \sin\alpha_1\sin\beta_1 & \cos\alpha_1 \end{bmatrix} \\ l_2 = \begin{bmatrix} \sin\alpha_2\cos\beta_2 & \sin\alpha_2\sin\beta_2 & \cos\alpha_2 \end{bmatrix} \end{cases} \quad (3)$$

with

$$\begin{cases} \alpha_1 = \alpha_2 = \alpha = \dfrac{\pi}{6} \\ \beta_1 = +\dfrac{\pi}{2} \\ \beta_2 = -\dfrac{\pi}{2} \end{cases} \quad (4)$$

Using the Lambertian reflectance map (Horn, 1986) we obtain

$$\begin{cases} I_1 = R_1(p,q) = L_0\rho\,\dfrac{-q\sin\alpha+\cos\alpha}{\sqrt{1+p^2+q^2}} \\ I_2 = R_2 = L_0\rho\,\dfrac{q\sin\alpha+\cos\alpha}{\sqrt{1+p^2+q^2}} \end{cases} \quad (5)$$

where I1 and I2 are the images, p and q are surface derivative along x and y respectively, L0 is the light source magnitude and ρ is the surface albedo. Solving for q, we obtain:

$$q(x,y) = \frac{1}{\tan\alpha}\,\frac{I_2(x,y)-I_1(x,y)}{I_2(x,y)+I_1(x,y)} \quad (6)$$

In this way, we can recover the surface derivative value in one direction. Note that although this derivative along y is exactly recovered, the estimation of the other component of the surface gradient with just a pair of images is not possible without making some assumption on p, such as convexity or smoothness assumptions.

To solve for the misalignment, we assume, for now, that most of our scanned photograph is flat (q=0). We find the best alignment minimizing the function

$$\sum_{i=1}^{N}\sum_{j=1}^{M}\left|q_{i,j}^{us}\right| = \sum_{i=1}^{N}\sum_{j=1}^{M}\left|\frac{1}{\tan\alpha}\,\frac{I_2^{us}{}_{i+\Delta i,j+\Delta j}-I_1^{us}{}_{i,j}}{I_2^{us}{}_{i+\Delta i,j+\Delta j}+I_1^{us}{}_{i,j}}\right| \quad (7)$$

where $I_{1,2}^{us}$ and q^{us} are the gray level upsampled images and scanned surface derivative along y,

$(\Delta i,\Delta j)$ is the misalignment and N and M are respectively the number of rows and columns. We used upsampled images to compute subpixel misalignments. After correcting the misalignment, we downsample images to their original resolution.

Figure 6: UL: Scanned image. UR: Repaired image. LL: Absolute value of the y derivative before the alignment step. LR: After alignment.

Fig.6 shows the derivative along y before and after the alignment step. We can see, in Fig. 6 LL, that there are some image edges that should not be in an albedo independent signal (such as the surface gradient), while such image content dramatically decreases after the images are aligned as shown in Fig. 6, right.

After the color transformation and alignment operations, these two source images can be used as input to compute a defect map that will indicate where tears and creases on the surface of the photograph are present. Unfortunately, the q image recovered at this point suffers from numerical noise in regions where the colors are dark (fall near the origin if the RGB color cube). Fig. 7 shows how the darkest square is noisier than the others, while the brightest gray one on the bottom right is practically invisible. Recall that our goal (regarding the repairing task) is to differentiate pixels associated with tears and creases from flat regions of the photograph, not necessarily to recover exact estimates of the gradient component. To this end, we have found it useful to combine the gradient and color difference information to define a composite image which is the normalized version of the product of the color differences multiplied by the

$$\hat{m}(x,y) = \frac{m(x,y)}{\max[m(x,y)]} \qquad (8)$$

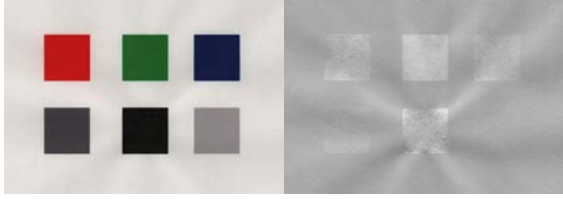estimated vertical derivative:

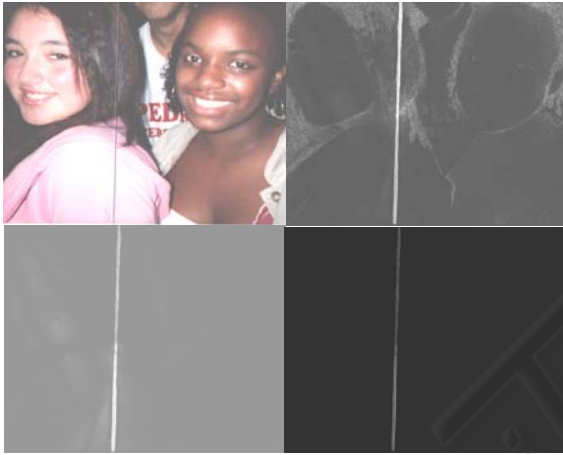Figure 7: Left: Scanned image; Right: Recovered gradient component along y.

Figure 8: UL: Scanned image. UR: Gradient component absolute value along x. LL: Absolute value of the difference between the two acquired images. LR: Mask $\hat{m}(x,y)$ is the input of the defect trimap generation step.

$$m(x,y) = |I_2(x,y) - I_1(x,y)| \cdot |q(x,y)| \qquad (9)$$

The gray level difference image has a value near zero where q is near zero and doesn't contain numerical errors due to the albedo. This feature is useful to eliminate the numerical errors in q, even if it adds some albedo dependent signal in regions containing defects. Note that we could still have a problem if a defect pixel has dark albedo. In practice we find that for these pixels, even if the (I_1, I_2) vector has a low magnitude, the difference of its components is big enough to distinguish the defect. In Fig.8 we can compare the gradient and difference images. While the noise in the gradient image is evident (we can distinguish the outline of the faces), the difference image has almost no numerical noise. Note that the defective pixels are also less visible in the difference image, but are enhanced in the composite image, m, due to the strong signal in the gradient. In short, we have used the gradient to enhance the signal in defect regions and use the difference image to avoid noise in the flat zones. Note that in figure 8 we display the scanned images rotated 90 degrees for clarity, effectively placing the light sources to the left and right in the figure.

Fig.8 LR shows the mask $\hat{m}(x,y)$ computed from the source images. This obtained mask has gray level values that must be thresholded in some way to decide how high the value must be to identify a defect pixel. A single threshold across all photos fails to be adequately robust. To this end, we define a function $\widetilde{m}$:

$$\widetilde{m}(x,y,\gamma) = \begin{cases} 0 \to \hat{m}(x,y) < \gamma \\ 1 \to \hat{m}(x,y) \geq \gamma \end{cases} \qquad (10)$$

This function is simply a binary image, with γ as threshold. The percentage of the image lying above this threshold is simply

$$A(\gamma) = \frac{1}{NM} \iint \widetilde{m}(x,y,\gamma) dxdy \qquad (11)$$

where N and M are respectively rows and columns number.

We compute a trimap by classifying each pixel as being either 'defect', 'uncertain' or 'non-defect'. We choose the 2 thresholds for this classification by finding the knee in the relationship between A and γ. Specifically, we set two thresholds on the angle the curve makes, namely $-\pi/8$ and $-3\pi/8$ which are 25% and 75% respectively of the angular range. A concrete example may clarify this approach. Fig.9 shows the function $A(\gamma)$ for the sample in fig.8. This is a display of the image area as a function of threshold γ. Choosing the angle thresholds above corresponds to γ thresholds of 0.005 and 0.0094 for constructing the tri-map. Fig.10 shows the trimap in which red pixels are defect, bright grey pixels are non-defect and black pixels are the unknown ones. In this example the defects are fairly easy to detect yielding a small number of unknown pixels.

Once such a trimap is constructed we need to classify the unknown pixels. For this we use Quadratic Discriminant Analysis (QDA) (Hastie et al., 2001). As features we use the q and difference images as well as the following image:

$$f(x,y) = \frac{\left|\rho(x,y) - \frac{E_1(x,y)}{\cos\alpha}\right| + \left|\rho(x,y) - \frac{E_2(x,y)}{\cos\alpha}\right|}{2} \qquad (12)$$
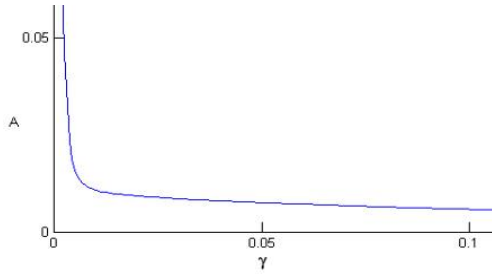
Figure 9: The function $A(\gamma)$ for Fig. 8a.

Figure 10: The trimap for Fig. 8a: red pixels are defect, light grey are non-defect and black are unknown (appear sparse and small in this case).

This equation is derived from eq. 5 by setting L_0 to 1 and $p(x,y)$=0. After normalizing, *f(x,y)* has low values in the non-defect pixels and high values (albedo dependent) in the defect pixels. Note that we have computed the albedo using classical photometric stereo methods and assuming p=0. Although in practice the unknown p does not always equal zero, especially for defective pixels, this assumption still yields the function, f(x,y), which is useful in distinguishing defect from non-defect pixels.

We apply QDA, trained on the known defect and non-defect pixels, and applied to the unknown pixels, for each photograph independently. This yields a labeling of all pixels as being either defective or not, which along with the albedo image, is processed by the refinement step, as described in 4.1. We use the albedo instead of one of the original images because some low frequency creases are removed by simply computing the albedo, even when they are present in the source images, as shown in Figure 11. We also apply the infilling procedure to the albedo image, not one of the original source images, since the albedo image is not prone to darkening introduced by the interaction of the non-perpendicular lights and subtle low frequency curvature on the surface of the photograph. Fig.12 shows the automatically detected defect map, which is the input for the refinement

step and the repaired image after the infilling algorithm.

Figure 11: Subtle, low frequency creases are avoided in the albedo image. Left: Scanned image. Middle: Recovered albedo. Right: repaired image.
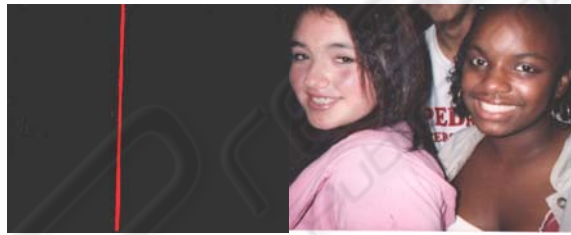

Figure 12: Left: Defect map before refinement step. Right: Repaired image after infilling algorithm.

Methods do exist in the literature that attempt to compute all gradient information from two images (Onn et al., 1990) (Tu et al., 2003) (Yang et al., 1992) (Petrovic et al., 2001). Unfortunately, after prototyping several of these, we find them insufficiently robust in practice.

5 INFILLING ALGORITHMS

The input to the infilling algorithm is a digital image in which every pixel is classified as either defective or non-defective. The non-defective pixels can be further classified as candidates or non-candidates for replication. A data structure is provided in which defective pixels are arranged in connected components.

Our algorithm essentially replaces every defective pixel by a value computed from selected candidate pixels. A candidate pixel may be any non-defective pixel of the image. The selection is based on (1) the spatial distance between the defect location and the candidate location and (2) the similarity of pixel values in the local neighborhoods of the two pixels. Two parameters govern the selection: the width W of a square region around the defect in which candidates are examined and the width w of a square local neighborhood surrounding

and including a pixel. Typically, the region width W is much greater than the neighborhood width w. For example, we used a region of 200×200 pixels and neighborhoods of 7×7, 9×9, and 11×11 pixels.

As a pre-processing step, we compute texture descriptors of all the local neighborhoods of candidate pixels in the image. In our implementation, we used mean and standard deviation of values in a surrounding w×w neighborhood as texture descriptors. The computations are done once for every candidate pixel and do not depend on any defective context. Pixel reconstruction is done for groups of connected components sequentially. The recommended order of pixel reconstruction within a single connected component is from the outside in. This order of computation creates fewer image artifacts. To reconstruct a defective pixel, we examine its surrounding w×w neighborhood while ignoring defective pixels in that neighborhood. The texture measures of the local neighborhood are computed, namely the mean and standard deviation of the non-defective pixel values. We then find 10% of the candidates in the W×W region around the defect whose texture measures best match the texture measures of the target neighborhood. To accelerate the search for the best 10% of all candidates, we use an efficient data structure where all the candidates in a region are sorted by both the mean and the standard deviation of their surrounding w×w neighborhoods.

For each of the 10% of selected candidate pixels, we further compare its w×w neighborhood relative to the defective pixel and its neighborhood. Neighborhoods are compared by the sum of squared differences (SSD) of respective values. Two approaches were used to compute the output pixel value, resulting in two different algorithms. The first approach, which is based on (Efros and Leung, 1999), takes the best pixel, i.e. lowest SSD. The second approach computes a weighted average of all the candidates, where the weighting is based on the SSD measure as follows. Let $Q = q_1, q_2, \ldots, q_{w \cdot w}$ be the two dimensional neighborhood surrounding the pixel to repair and let C be the set of candidate neighborhoods. For a neighborhood P in C, we use the notation $P = p_1, p_2 \ldots, p_{w \cdot w}$ and denote its central pixel by p. Let $G = g_1, g_2 \ldots, g_{w \cdot w}$ be a Gaussian spatial filter, and let h be a real value weight filter. For a defective pixel i in the neighborhood P, the corresponding value of the Gaussian filter g_i is set to 0. The new value for the pixel is:

$$\bar{q} = \frac{\sum_{p \in C} \exp(\frac{-\sum_{i=0}^{w \cdot w} g_i \cdot (p_i - q_i)^2}{h^2}) \cdot p}{\sum_{p \in C} \exp(\frac{-\sum_{i=0}^{w \cdot w} g_i \cdot (p_i - q_i)^2}{h^2})} \quad (13)$$
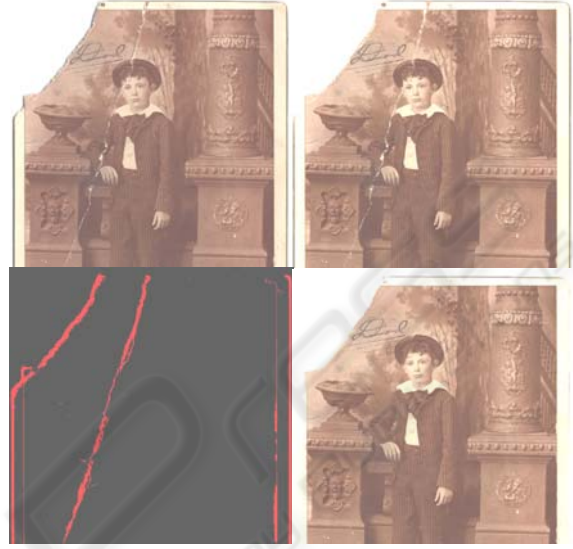

Figure 13: UL: scanned image. UR: albedo. LL: automatically computed defect map before refinement. LR: repaired image using infilling algorithms.

This method is adapted from the NL-Means denoising algorithm (Buades et al., 2005). By applying SSD comparisons to only 10% of the candidate neighborhoods instead of all the neighborhoods in the surrounding region, we attain approximately a factor of ten speed up, and no visible degradation in image quality. This speed up makes these algorithms applicable in practical infilling tasks, as those described in subsequent sections.

Note that the accelerated infilling algorithms are still slower than simple local operations such as median filtering or averaging. These local algorithms however tend to blur image details, so they are not acceptable for a photo repair application. Fig.13 shows the entire automatic procedure (using two images, the automatic defect detection, the refinement procedure and the infilling algorithm) for the photograph in fig.1.

6 ADDITIONAL APPLICATIONS

In addition to allowing the repair of old photographs, the combination of color and normal or reflectance data taken from physical objects can be applied in

other ways. Transforming reflectance data based on normal information to enhance surface perception of detail has already been demonstrated (Malzbender et al., 2001), (Toler-Franklin et al., 2007), (Freeth et al., 2006). A further example on data captured by our flatbed scanner is shown in fig. 14. Combing multiple images taken under multiple lighting in a spatially varying manner can also yield enhanced visualizations (Fattal et al., 2007). Data captured from our scanners can also be used for these methods. Lastly, normal information from photometric stereo can of course be integrated to recover a 3D model of surface structure (Horn, 1986). This geometry will typically suffer from a number of artifacts, such as low-frequency warping from the integration of inaccuracies and mishandling of discontinuities in the object geometry.

7   CONCLUSIONS

We have presented a technique to recover the 3D normal structure of an object using a conventional flatbed scanner. This allows relighting, and limited geometry capture. We have also demonstrated an application to the automatic repair of damaged photographs exhibiting creases or tears. Although we prototyped this functionality on a particular HP scanner, the approach is applicable to any flatbed scanner that uses 2 bulbs to illuminate the platen, which is the common case.

Outstanding challenges still remain. First, the depth of geometry we can handle is limited by the optics of the scanner. For the unmodified scanners we used in our work, we measured this to be approximately 1 cm. Second, a geometric warp must be applied to the raw scanner data to rectify the images before registration. This must be done to sub-pixel accuracy to obtain reliable normal estimates. Also, a limitation of the 2 image approach we have taken (but not our 4 image approach) is our inability to detect perfectly aligned defects. This can however be accommodated in most cases by the user simply avoiding such defects with a rotation of the photograph to re-align it.

We have investigated techniques in the literature that attempt to recover both surface derivatives components, (p,q), from a single pair of images, but have found them insufficiently robust. In future work, we would like to develop such a robust method.
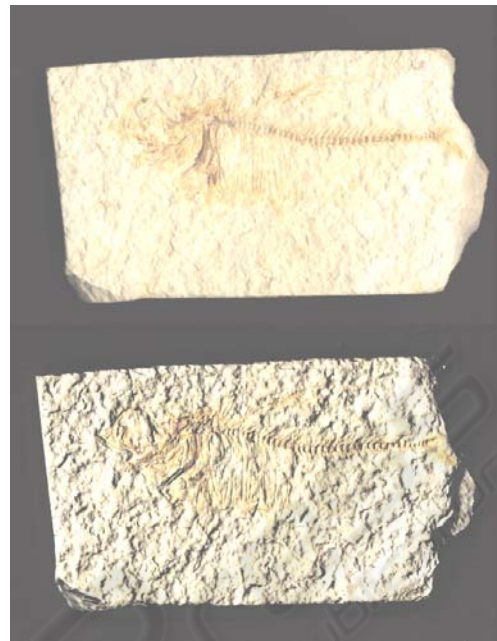

Figure 14: Top: The first of the four scans shown in Fig. 3. Bottom: Interactively relit to enhance surface detail.

ACKNOWLEDGEMENTS

REFERENCES

Barsky, S., and Petrou, M. 2003. The 4-Source Photometric Stereo Technique for Three-Dimensional Surfaces in the Presence of Highlights and Shadows, IEEE Transaction on Pattern Analysis and Machine Intelligence, Vol. 25, No. 10, pp. 1239-1252.

Bergman, R., Maurer, R., Nachlieli, H., Ruckenstein, G., Chase, P., and Greig, D. 2007. Comprehensive Solutions for Automatic Removal of Dust and Scratches from Images, Journal of Electronic Imaging.

Brown, B., Toler-Franklin, C., Nehad, D., Burns, M., Dobkin, D., Vlachopoulos, A., Doumas, C., Rusinkiewicz, S., Weyrich, T., "A System for High-Volume Acquisition and Matching of Fresco Fragments: Reassembling Theran Wall Paintings",

ACM Transactions on Graphics, Vol. 27, No. 3, pp.83:1-9, August 2008.

Buades, A., Coll, B., and Morel, J. 2005. A Review of Image Denoising Algorithms, With a New One, Multiscale Modeling and Simulation (SIAM interdisciplinary journal), Vol 4 (2), pp. 490 - 530.

Chantler, M., and Spense, A. 2004. Apparatus and Method for Obtaining Surface Texture Information, Patent GB 0424417.4.

DIGITAL ICE™, Eastman Kodak Company, http://asf.com/products/ice/FilmICEOverview/.

Efros, A., and Leung, T. 1999. Texture Synthesis by Non-parametric Sampling. In Proceedings of IEEE Internation Conference on Computer Vision, September.

Fattal, R., Agrawala, M., and Rusinkiewicz, S. 2007. Multiscale Shape and Detail Enhancement from Multiple-light Image Collections, ACM Transactions on Graphics, 26 (3).

Freeth, T., Bitsakis, Y., Moussas, X., Seiradakis, J., Tselikas, A., Mangou, H., Zafeiropoulou, M., Hadland, R., Bate, D., Ramsey, A., Allen, M., Crawley, A., Hockley, P., Malzbender, T., Gelb, D., Ambrisco, W., and Edmunds, M. 2006. Decoding the Ancient Greek Astronomical Calculator known as the Antikythera Mechanism, Nature, Vol. 444, Nov. 30, pp. 587 – 591.

Gardner, A., Tchou, C., Hawkins, T., and Debevec, P. 2003 Linear Light Source Reflectometry, ACM Transactions on Graphics, Vol. 22, No. 3, pp. 749-758.

Hammer, O., Bengston, S., Malzbender, T., and Gelb, D. 2002. Imaging Fossils Using Reflectance Transformation and Interactive Manipulation of Virtual Light Sources, Palaeontologia Electronica · August 23.

Hastie, T., Tibshirani, R., and Friedman, J. 2001. The Elements of Statistical Learning - Data Mining, Inference, and Prediction. Springer-Velag.

Hewlett-Packard G4050 Photo Scanner, 2007. www.hp.com.

Horn, P. 1986. Robot Vision, MIT Press, ISBN 0-262-08159-8.

Klette, R., Schluns, K., and Koschan, A. 1998. Computer Vision: Three-Dimensional Data from Images, Springer –Verlag.

Kschischang, F. R., Frey, B. J., and Loeliger, H. A. 2001. Factor Graphs and the Sum-Product Algorithm, IEEE Transaction on Information Theory, Vol. 47, No. 2.

Malzbender, T., Gelb, D., and Wolters, H. 2001. Polynomial Texture Maps. In Proceedings of ACM Siggraph 2001, ACM Press / ACM SIGGRAPH, New York. E. Fiume, Ed., Computer Graphics Proceedings, Annual Conference Series, ACM, 519-528.

Medioni, G., Lee,M., and Tang, C. 2000. A Computational Framework for Segmentation and Grouping, Elsevier.

Onn, R., and Bruckstein, A. 1990 Integrability Disambiguates Surface Recovery in Two-Image Photometric Stereo, International Journal of Computer Vision, vol. 5, pp. 105-113.

Petrovic, N., Cohen, I., Frey, B. J., Koetter, R., and Huang, T. S. 2001. Enforcing Integrability for Surface Reconstruction Algorithms Using Belief Propagation in Graphical Models, 2001 IEEE Conf. on Computer Vision and Pattern Recognition, vol. 1, pp. 743-748.

Schubert, R. 2000. Using a Flatbed Scanner as a Stereoscopic Near-Field Camera, IEEE Computer Graphics and Applications, pp. 38-45.

Toler-Franklin, C., Finkelstein, A., and Rusinkiewics, S. 2007. Illustration of Complex Real-World Objects using Images with Normals, International Symposium on Non-Photorealistic Animation and Rendering.

Tu, P., and Mendonca, P. R. S., 2003. Surface Reconstruction via Helmholtz Reciprocity with a Single Image Pair, Proc. of 2003 IEEE Computer Society Conference on computer Vision and Pattern Recognition (CVPR'03), pp. 541-547.

Yang, J., Ohnishi, N., and Sugie, N. 2003. Two Image Photometric Stero Method, Proc. SPIE, Intelligent Robots and Computer Vision XI, Vol. 1826, pp. 452-463.